



## Article

# Coastline Monitoring and Prediction Based on Long-Term Remote Sensing Data—A Case Study of the Eastern Coast of Laizhou Bay, China

Ke Mu <sup>1,2,3</sup>, Cheng Tang <sup>1,2,\*</sup> , Luigi Tosi <sup>4</sup> , Yanfang Li <sup>1,2</sup> , Xiangyang Zheng <sup>1,2</sup>, Sandra Donnici <sup>4</sup> , Jixiang Sun <sup>1,2,3</sup>, Jun Liu <sup>5</sup> and Xuelu Gao <sup>1,2</sup>

- <sup>1</sup> CAS Key Laboratory of Coastal Environmental Processes and Ecological Remediation, Yantai Institute of Coastal Zone Research, Chinese Academy of Sciences, Yantai 264003, China; muke21@mails.ucas.ac.cn (K.M.); yfli@yic.ac.cn (Y.L.); sunjixiang22@mails.ucas.ac.cn (J.S.); xlgao@yic.ac.cn (X.G.)
- <sup>2</sup> Shandong Key Laboratory of Coastal Environmental Processes, Yantai 264003, China
- <sup>3</sup> University of Chinese Academy of Sciences, Beijing 100049, China
- <sup>4</sup> Institute of Geosciences and Earth Resources, National Research Council, 35131 Padova, Italy; luigi.tosi@igg.cnr.it (L.T.); sandra.donnici@igg.cnr.it (S.D.)
- <sup>5</sup> Yantai Center of Coastal Zone Geological Survey, China Geological Survey, Yantai 264001, China
- \* Correspondence: ctang@yic.ac.cn

**Abstract:** Monitoring shoreline movements is essential for understanding the impact of anthropogenic activities and climate change on the coastal zone dynamics. The use of remote sensing allows for large-scale spatial and temporal studies to better comprehend current trends. This study used Landsat 5 (TM), Landsat 8 (OLI), and Sentinel-2 (MSI) remote sensing images, together with the Otsu algorithm, marching squares algorithm, and tidal correction algorithm, to extract and correct the coastline positions of the east coast of Laizhou Bay in China from 1984 to 2022. The results indicate that 89.63% of the extracted shoreline segments have an error less than 30 m compared to the manually drawn coastline. The total length of the coastline increased from 166.90 km to 364.20 km, throughout the observation period, with a length change intensity (LCI) of 3.11% due to the development of coastal protection and engineering structures for human activities. The anthropization led to a decrease in the natural coastline from 83.33% to 13.89% and a continuous increase in the diversity and human use of the coastline. In particular, the index of coastline diversity (ICTD) and the index of coastline utilization degree (ICUD) increased from 0.39 to 0.79, and from 153.30 to 390.37, respectively. Over 70% of the sandy beaches experienced erosional processes. The shoreline erosion calculated using the end point rate (EPR) and the linear regression rate (LRR) is 79.54% and 85.58%, respectively. The fractal dimension of the coastline shows an increasing trend and is positively correlated with human activities. Coastline changes are primarily attributed to interventions such as land reclamation, aquaculture development, and port construction resulting in the creation of 10,000.20 hectares of new coastal areas. Finally, the use of Kalman filtering for the first time made it possible to predict that approximately 84.58% of the sandy coastline will be eroded to varying degrees by 2032. The research results can provide valuable reference for the scientific planning and rational utilization of resources on the eastern coast of Laizhou Bay.

**Keywords:** spatiotemporal changes; coastal erosion; shoreline extraction; DSAS; Google Earth Engine; Laizhou Bay



**Citation:** Mu, K.; Tang, C.; Tosi, L.; Li, Y.; Zheng, X.; Donnici, S.; Sun, J.; Liu, J.; Gao, X. Coastline Monitoring and Prediction Based on Long-Term Remote Sensing Data—A Case Study of the Eastern Coast of Laizhou Bay, China. *Remote Sens.* **2024**, *16*, 185. <https://doi.org/10.3390/rs16010185>

Academic Editor: Jorge Vazquez

Received: 27 November 2023

Revised: 11 December 2023

Accepted: 13 December 2023

Published: 1 January 2024



**Copyright:** © 2024 by the authors. Licensee MDPI, Basel, Switzerland. This article is an open access article distributed under the terms and conditions of the Creative Commons Attribution (CC BY) license (<https://creativecommons.org/licenses/by/4.0/>).

## 1. Introduction

Global land- and ocean-dominated natural and induced processes combine and interact in the transition zone between the land and the sea. The reaction to this interaction is reflected in the long- and short-term changes in the coastline [1]. Climate change and human activities make coastal areas increasingly vulnerable to flooding and coastal erosion,

with significant impacts on socio-economic conditions [2,3], ecosystem degradation [4–6], the ecological environment [7–9], and landscape changes [10–12]. In coastal planning and management, the monitoring and prediction of coastline changes are of great importance [13–16], as they help understand processes such as erosion, sedimentation, and sea level rise and make decisions [17,18].

Over the last decade, significant progress has been made in the field of remote sensing (RS) [19] thanks to the continuous availability of new platforms equipped with various sensors, the development of new algorithms for data processing and the support of increasingly powerful geographic information systems (GIS), cloud platforms, and machine learning techniques. Studies of coastal areas have benefited greatly from RS, especially those focusing on coastline dynamics, because of the advantages of more continuous data coverage, high accuracy, near real time data availability, and cost-effectiveness [20–23].

As a cloud platform, Google Earth Engine (GEE) provides developers with extensive data resources and powerful computational capabilities, as well as flexible tools for data analysis and visualization. The use of Google Earth Engine (GEE) is a good compromise in terms of long time series data, accuracy and resolution, and revisiting time for monitoring coastal changes with large coverage. As a result, an increasing number of people are using GEE to monitor long-term changes in coastlines [21,24–26].

Laizhou Bay, which lies south of the Bohai Sea and on the northern side of the Shandong Peninsula, is part of China's Bohai Sea Economic Rim. Previous studies on this region have shown that Laizhou Bay has undergone significant coastal changes over the last half century. These changes are mainly due to human activities, such as land reclamation, aquaculture development, and beach sand mining [27–29], resulting in a decrease of 1253.2 km<sup>2</sup> in the marine area, which mainly occurred in the last 40 years [27]. Specifically, the eastern part of Laizhou Bay, which is largely characterized by a sandy coastline, has suffered severe erosion. In contrast, the western part at the mouth of the Yellow River, mostly formed by a muddy coast, no recognizable changes in the shoreline have been revealed [27,30]. Most previous studies relied mainly on the visual interpretation of the coastline extraction, or considered the instantaneous waterline shown on satellite images as the actual position of the coastline, and no results on long-term coastal changes were presented [27].

The aim of this study is to take a step forward in the long-term analysis of the spatiotemporal characteristics of coastline changes and the associated driving forces on the eastern coast of Laizhou Bay. An automated procedure was developed to extract and correct the positions of the coastline based on nine satellite images spanning from 1984 to 2022 and available from GEE. The modified normalized difference water index (MDNWI) combined with the Otsu method was used together with a tidal model. The integrated analysis of the coastline changes was based on calculating specific indices, while Kalman filtering [31,32], applied here for the first time, was used to predict the coastline change for the year 2032. To summarize, compared to previous studies, here we used a large dataset of RS images, new coastline extraction methods achieving relatively low errors, and Kalman filtering to predict the evolution of the sandy coastline. This enabled us to analyze this region more comprehensively than before.

## 2. Materials and Methods

### 2.1. Study Area

The study area is the eastern part of Laizhou Bay, which is located northwest of the Shandong Peninsula, south of the Bohai Sea (37°11'23"N to 37°41'54"N and 119°44'58"E to 120°20'08"E). More precisely, it is the coastline that stretches from northeast to southwest, between Qimu Island and Hutouya. Qimu Island is a sandy spit of land bordering the northern part of Longkou Bay and the Longkou Artificial Island (Yantai Province). Sanshan Island and Diaolongju are in the middle of the study area. The most important watercourses flowing directly into the coastal section under investigation are the Wang and Jie rivers. In addition, there is the Yellow River, which, although its mouth is in the west, influences the southern part of the studied coast. The coastal strip from Qimu Island to Diaolongju

consists mainly of sandy beaches characterized by the upper modern deposits of a yellow-brown alluvial fine sand layer and lower lagoon facies of yellow-green and dark gray fine sand, silt, and clay layers (Figure 1).

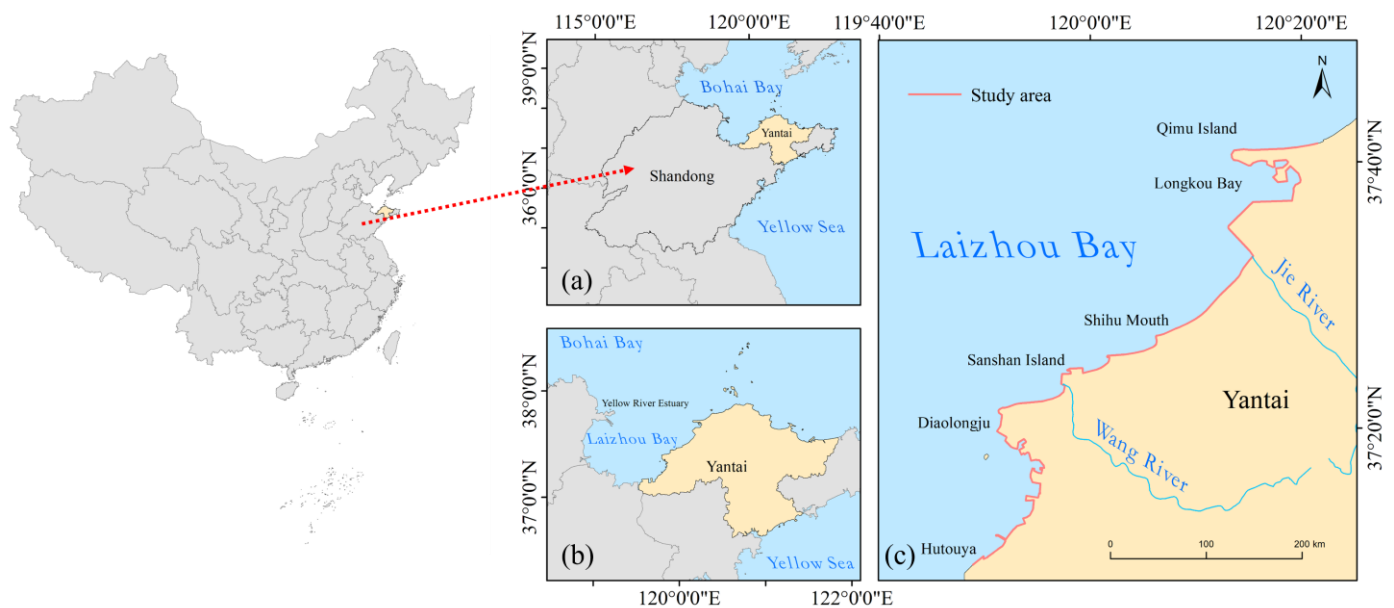


**Figure 1.** Regional framework of the study area: (a) Bohai Bay and Shandong Province; (b) Laizhou Bay and Yantai. (c) The analyzed coastline.

The study area is characterized by an irregular mixed semi-diurnal tide. The residual currents near Longkou Bay and Sanshan Island have velocities between 0.01 and 0.03 m/s. The distribution of residual currents is generally consistent with the distribution of tidal currents. In the sector of Longkou Bay (Longkou Wave Observation Station), the strong wind directions in the region are NNE and NE, with a maximum wind speed of 20 m/s. The prevailing wind direction is south, with a frequency of 15%. The wind waves are 90% with a predominant NE direction, an average wave height of 0.6 m (height 7.2 m), and a frequency of 14%. In the Sanshan sector (Sanshan Island Wave Observation Station) wind waves predominate with a predominant NNE direction, an average wave height of 1.3 m (maximum height 3.9 m), and a frequency of 11%.

## 2.2. Data Sources

The remote sensing data sets originate from GEE and comprise the atmospherically corrected TOA (top of atmosphere) data from the Landsat 5 (TM), Landsat 8 (OLI), and Sentinel-2 (MSI) sensors. An interval of five years was chosen between the satellite images, except for 2012, which was replaced by 2011 due to the lack of Landsat images. Specifically, the selected images refer to the years 1984, 1987, 1992, 1997, 2002, 2007, 2011, 2017, and 2022. The criteria for image selection were primarily low cloud coverage and clear land-water boundaries. The CoastSat toolkit was used to calculate the percentage of cloud cover and to filter the images with a threshold of 5% [33]. The visible bands (red, green, blue), the near-infrared band (NIR), and the shortwave infrared band (SWIR 1) were used for shoreline extraction and the “min\_size” value in CoastSat was adjusted to maximize the selection of original images that meet the criteria. Landsat 5 images with 30 m resolution were upsampled to 15 m by bilinear interpolation. A data fusion method based on the principal component was used for Landsat 8 (OLI) images. The multispectral bands with a resolution of 30 m were upsampled to 15 m using the panchromatic 15 m band [34]. For the Sentinel-2 images, the 20 m SWIR 1 bands was upsampled to 10 m resolution by bilinear interpolation.

The yearbooks of the local authorities of the surrounding towns, such as sand mining, land use, coastal engineering development, and economic information, were used to analyze the causes of the changes in the coastline.

### 2.3. Extraction of the Coastline Position

The modified normalized difference water index (MNDWI) [35] in combination with the Otsu algorithm [36] is used to extract the instantaneous waterline. The mathematical expression is:

$$\text{MNDWI} = \frac{L_{\text{Green}} - L_{\text{MIR}}}{L_{\text{Green}} + L_{\text{MIR}}}, \quad (1)$$

where  $L_{\text{Green}}$  and  $L_{\text{MIR}}$  represent the pixel brightness values in the green and mid-infrared (MIR) bands, respectively. The shortwave infrared 1 (SWIR1) band is used to correspond to the MIR band. For water bodies, their MNDWI values are generally greater than 1, and for non-water bodies, they are less than 1.

Using the Otsu algorithm and combining it with the water and non-water grid generated by a neural network model, we obtain the optimal segmentation threshold for water and non-water on the MNDWI image. Once the threshold for segmentation is determined, the marching squares algorithm is used to extract the contour line corresponding to this threshold on the MNDWI image under the subpixel resolution. This contour line represents the instantaneous water boundary in the remote sensing image [33,37].

The extracted shoreline position represents the instantaneous water boundary recorded by the satellite sensor and not the actual coastline at the MHWL, i.e., the intersection of the plane of the MHW tidal datum with the shore. Therefore, a tidal correction is performed to determine the actual coastline position (Figure 2).

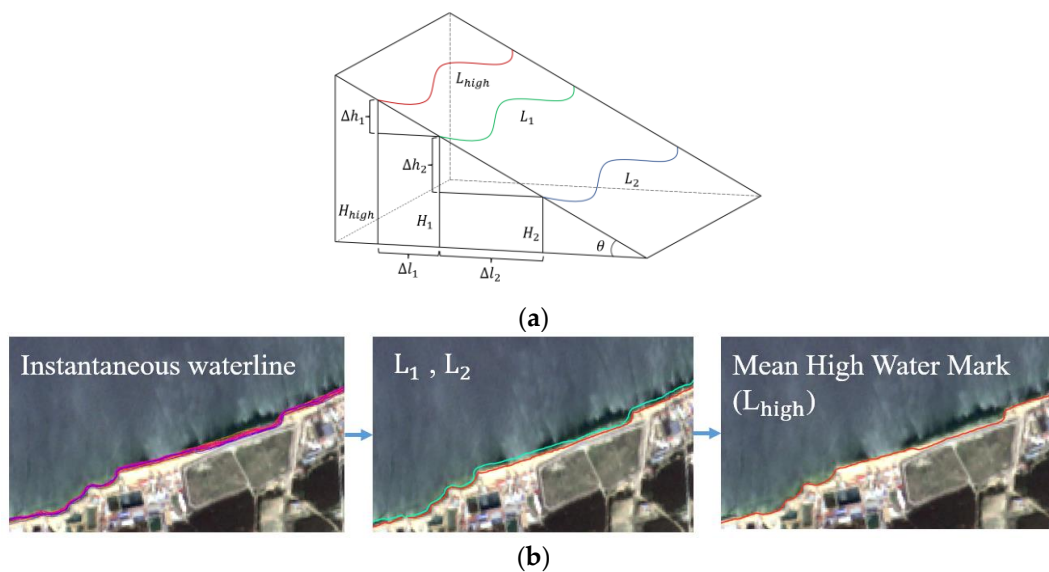


**Figure 2.** (a) Tidal correction schematic diagram:  $L_1$  and  $L_2$  represent the instantaneous water boundary extracted at two different time points and  $L_{\text{high}}$  is the position of the average high tide line,  $H_1$ ,  $H_2$ , and  $H_{\text{high}}$  refer to the corresponding tide levels for  $L_1$ ,  $L_2$ , and  $L_{\text{high}}$ ,  $\theta$  is the slope angle of the beach.  $\Delta h$  is tidal range.  $\Delta l$  is vertical distance; (b) schematic diagram of the coastline correction process (The bottom image shows the image of Sentinel-2 in 2022).

According to the tidal range  $\Delta h_1$  and  $\Delta h_2$ , as well as the vertical distance  $\Delta l_2$  between the two instantaneous coastlines, the correction distance  $\Delta l_1$  is calculated as:

$$\Delta l_1 = \Delta l_2 \times \frac{\Delta h_1}{\Delta h_2}. \quad (2)$$

Due to the lack of long-term tidal measurements, the Finite Element Solution 2014 global tidal model (FES2014) [38] is used to simulate tidal data per 15-min interval from 1984 to 2022. FES2014 provided the values of  $H_1$  and  $H_2$ . The high water levels during each spring tide period (with the largest tidal range) for three consecutive days and calculated their average value, which was taken as the  $H_{\text{high}}$  value. To ensure the accuracy of the coastline extraction, the study area was divided into 6 subregions. A total of 1300 available remote sensing images were selected. For each year's coastline, two images with significant tidal differences within the same month or in neighboring months were selected to reduce the effects of seasonal variations and errors caused by image quality.

#### 2.4. Shoreline Classification

Considering the actual situation of the study area and the technical regulations for coastal surveying and mapping under the Special Marine Comprehensive Survey Project (Project 908), the shoreline was divided into three primary and nine secondary categories (Table 1) based on visual interpretation.

**Table 1.** Classification of shorelines and their intensity index.

Primary Classification	Secondary Classification	Intensity Index
natural coastline	sandy coastline	1
	bedrock coastline	1
	silty coastline	1
artificial coastline	construction of embankments	4
	harbor and wharf	5
	aquaculture embankments	3
	groynes	4
	artificial islands	5
estuarine coastline	estuary surface	2

For the subsequent analysis of the driving forces, different intensity indices are assigned to different types of coastlines. The intensity index for natural coastline is set to 1. Due to its uniqueness, the estuarine surface is distinguished from natural shorelines and set to 2. Aquaculture embankments, which have a relatively low impact on ecological changes, are set to 3. The construction of embankments and groynes are set to 4. Harbors, wharfs, and artificial islands, due to their construction often involving land reclamation and significant ecological impacts over a large area, are set to 5 (Table 1).

#### 2.5. Coastline Diversity

The diversity of coastline development patterns can be assessed by the ICTD (index of coastline type diversity) [39]:

$$ICTD = 1 - \frac{\sum_{i=1}^n L_i^2}{\left(\sum_{i=1}^n L_i\right)^2} \quad ICTD \in (0, 1), \quad (3)$$

where  $n$  represents the number of coastline types at Laizhou Bay and  $L_i$  is the coastline length of type  $i$ .

An ICTD value close to 0 indicates the presence of a single coastline type, whereas values close to 1 mean that the coastline types are complex, and the diversity is high. The ICTD is low if there are fewer coastline types and if the percentage of the length of one coastline type is significantly greater than that of the others.

This study combines the number and length of coastline types in the Laizhou Bay region for each corresponding year to analyze the changing trends and reasons for the ICTD.

## 2.6. Coastline Changes

Length change intensity (LCI), end point rate (EPR), and linear regression rate (LRR) represent the coastline changes [40–42].

The LCI is the annual average percentage change in the length of the coastline within a certain period. The mathematical expression is:

$$LCI_{ij} = \frac{L_j - L_i}{L_i(j - i)}, \quad (4)$$

where  $LCI_{ij}$  represents the intensity of coastline length change from year  $i$  to year  $j$ ,  $L_i$  and  $L_j$  are represents the coastline length in year  $i$ , and in year  $j$ , respectively. The closer the LCI value is to 0, the lower the intensity of shoreline length change. A positive and negative LCI indicate an increase and decrease in coastline length, respectively.

EPR and LRR are calculated through digital shoreline analysis system (DSAS) [43]. The EPR is calculated by dividing the distance the coastline has moved by the time between the most recent and the oldest coastlines. The mathematical expression of EPR is:

$$EPR_{m(i,j)} = \frac{D_{mi} - D_{mj}}{T_{m(i,j)}}, \quad (5)$$

where  $EPR_{m(i,j)}$  represents the end point rate of shoreline changes from profile  $i$  to  $j$ .  $D_{mi}$  and  $D_{mj}$  are the distances between the intersection points of the shoreline and profile at time  $i$  and time  $j$ , respectively, with respect to the baseline.  $T_{m(i,j)}$  represents the time interval between time  $i$  and time  $j$ .

The LRR is calculated by linear regression using the least squares method, fitting a line to the intersection points of the profile line and the shoreline. The slope of the fitted line represents the LRR of the shoreline at that location. The mathematical expression of LRR is:

$$y = a_m x + b_m, \quad (6)$$

$$b_m = \frac{n \sum_i^n x_i y_i - \sum_i^n x_i \sum_i^n y_i}{n \sum_i^n x_i^2 - (\sum_i^n x_i)^2}, \quad (7)$$

$$a_m = \frac{\sum_i x_i^2 \sum_i y_i - \sum_i x_i \sum_i x_i y_i}{n \sum_i x_i^2 - (\sum_i x_i)^2}, \quad (8)$$

where  $a_m$  represents the slope of the regression line for the intersection points on the  $m$ th profile,  $b_m$  is the intercept of the regression line for the intersection points,  $x_i$  is the  $x$ -coordinate value of the intersection point on the  $m$  profile at moment  $i$ ,  $y_i$  is the distance between the intersection point and the baseline on the  $m$ 'th profile at moment  $i$  ( $y$ -coordinate value), and  $n$  represents the number of intersection points between the profile and the shoreline.

## 2.7. Coastline Utilization

The degree of utilization can simply and effectively reflect the degree of impact of human activities on the ecological landscape, with utilization gradually increasing. The index of coastline utilization degree (ICUD) [44] is a comprehensive index that measures the extent of coastline utilization. Assigning different indices of human activity intensity to different coastal segments (Table 1). The mathematical expression of ICUD is:

$$ICUD = \sum_{i=1}^n (A_i \times C_i) \times 100, \quad (9)$$

where  $A_i$  represents the human impact intensity index of category  $i$  utilization,  $C_i$  represents the length percentage of category  $i$  utilization, and  $n$  represents the total number of shoreline types. A higher ICUD value indicates a higher level of human impact on the shoreline.

### 2.8. Coastline Complexity

The fractal dimension of a coastline refers to the length of the coastline and does not change with scale. It can reflect the degree of curvature and complexity of the coastline [45]. A higher fractal dimension indicates a higher degree of curvature and complexity of the coastline and can also reflect the intensity of human modification or the erosion and sedimentation status of the coastline. This study uses the grid method to calculate the fractal dimension of the coastline. The basic idea of the grid method is to cover the coastline with nonoverlapping square grids of different lengths. As the length of the grid square, denoted as  $r$ , changes, the number of grid squares  $N(r)$  covering the entire coastline changes accordingly. The relationship between them is:

$$N(r) \propto r^{-D}, \quad (10)$$

taking the logarithm of both sides of the equation:

$$\ln N(r) = -D \ln r + A, \quad (11)$$

where  $A$  is an unknown constant, and  $D$  is the measured fractal dimension of the coastline. A higher value for fractal dimension indicates a more complex shape of the coastline. Grid lengths from 10 m to 90 m are used in this study, with increments of 10 m. A total of 9 grid length indices was obtained for the corresponding grid lengths and the number of grids. The least squares method was employed for fitting and regression analysis to calculate the fractal dimension.

### 2.9. Prediction of Shoreline Evolution

A Kalman filter [31,32] was used to predict the future evolution of the shoreline by 2032 combining the observed shoreline with the modelled shoreline. The prediction recursion equations of the Kalman filter are generally derived using the orthogonal projection theorem and mathematical induction [46]:

$$\hat{X}(k+1|k+1) = \Phi(k+1, k)\hat{X}(k|k) + K(k+1)[Z(k+1) - H(k+1)\Phi(k+1, k)\hat{X}(k|k)], \quad (12)$$

$$K(k+1) = \frac{P(k+1|k)H^T(k+1)}{H(k+1)P(k+1|k)H^T(k+1) + R(k+1)}, \quad (13)$$

$$P(k+1|k) = \Phi(k+1, k)P(k|k)\Phi^T(k+1, k) + \Gamma(k+1|k)Q(k)\Gamma^T(k+1, k), \quad (14)$$

$$P(k+1|k+1) = [I - K(k+1)H(k+1)]P(k+1|k), \quad (15)$$

where  $\hat{X}(k+1|k+1)$  represents the state estimate at time  $k+1$ . The Kalman gain matrix at time  $k+1$  is denoted by  $K(k+1)$ . The state transfer matrix from time  $k$  to  $k+1$  is denoted by  $\Phi(k+1, k)$ . The incentive transfer matrix from time  $k$  to  $k+1$  is denoted by  $\Gamma(k+1|k)$ . The one-step ahead prediction error covariance matrix from time  $k$  to time  $k+1$  is denoted by  $P(k+1|k)$ . The error covariance matrix of the filtering prediction at time  $k+1$  is represented by matrix  $P(k+1|k+1)$ .  $Q(k)$  is the covariance matrix of the  $p$ -dimensional system noise vector, while  $R(k)$  is the covariance matrix of the  $m$ -dimensional measurement noise vector. "I" refers to the identity matrix.

The main steps for running a Kalman filter for shoreline prediction are as follows: From the earliest observed coastline, predict the position of the coastline for each subsequent time step until the next observed coastline is encountered. Whenever an observed coastline is encountered, the Kalman filter updates the velocity and uncertainty, aiming to minimize the error between the modelled coastline position and the observed coastline position. This helps to improve the accuracy of the predictions. After updating the velocity, the Kalman filter uses it to predict the position of the coastline for each subsequent time step until it encounters the next observed coastline. At that point, the new data is assimilated into the

model once again. This process is repeated until the desired forecast date is reached. The Kalman filter allows the rate of change of the coastline to vary over time, resulting in a better simulation and prediction of the coastline. It helps to distinguish the differences from long-term linear regression.

### 3. Results

#### 3.1. Coastline Accuracy Analysis

The accuracy of the positions of the extracted coastlines was assessed using a buffer analysis and an overlay analysis against the existing publicly available coastline dataset (EPACD) [22]. Buffers of 10 m, 15 m, 30 m, and 60 m were used to calculate the length of the extracted coastlines that fell within the buffer zones.

The global multiple scale shorelines dataset based on Google Earth Images 2015 (2015-Liu) [47], which includes the highest spatial resolution (<10 m) remote sensing images, was used to compare the shoreline automatically extracted in 2017. Validation results showed that 28.11% of the extracted shorelines have an error of  $\leq 10$  m, 21.63% an error of 10–15 m, 39.89% an error of 15–30 m, and 7.76% an error of 30–60 m. Only for 2.61% of the extracted shoreline did the error exceed 60 m (Figure 3). This indicates that the shoreline extracted using this method has good accuracy and can be used to analyze the spatiotemporal changes in the eastern shoreline of Laizhou Bay.

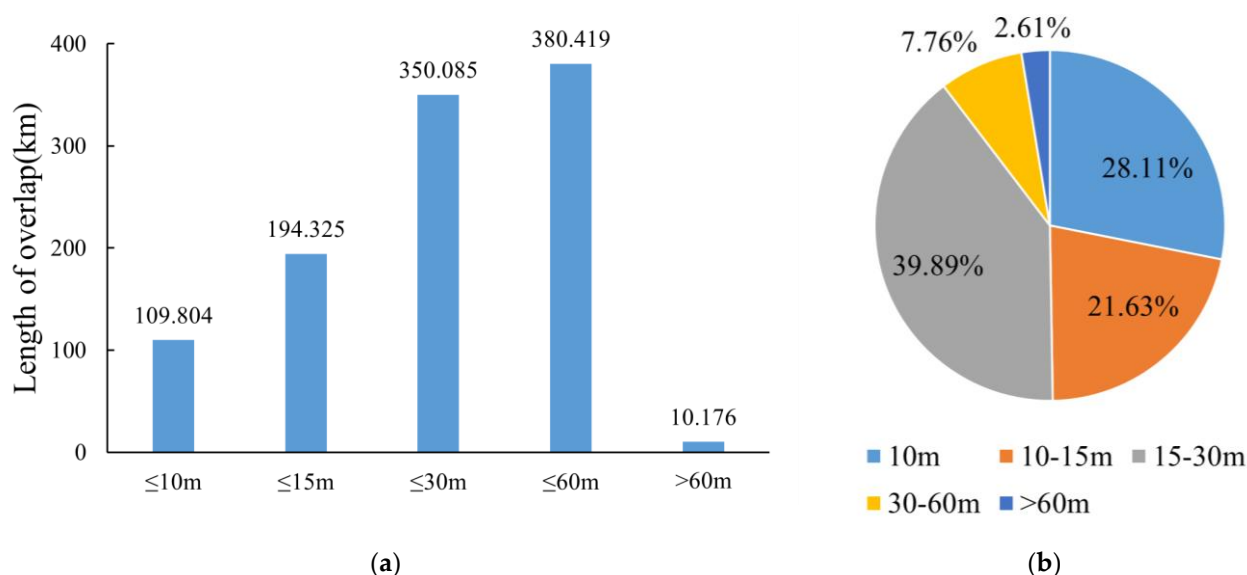


**Figure 3.** Results of the accuracy assessment of the extracted shorelines: (a) length of overlap in different buffer zone ranges; (b) proportion of overlap length.

#### 3.2. Analysis of Spatio-Temporal Changes in the Coastline

The extracted shorelines from nine periods were classified according to the classification criteria in Table 1. The lengths of the different types of the shorelines were then calculated for each corresponding year, resulting in the spatiotemporal distribution characteristics of shoreline types in the different periods (Figure 4). The results show that the shoreline length on the eastern coast of Laizhou Bay generally increased from 166.90 km to 364.20 km, between 1984 and 2022. The total length of natural shorelines shows a decreasing trend by 63.62% from 139.09 km in 1984 to 50.60 km in 2022. On the other hand, the total length of artificial shorelines increased by 1024.82% from 27.81 km in 1984 to 313.60 km in 2022.

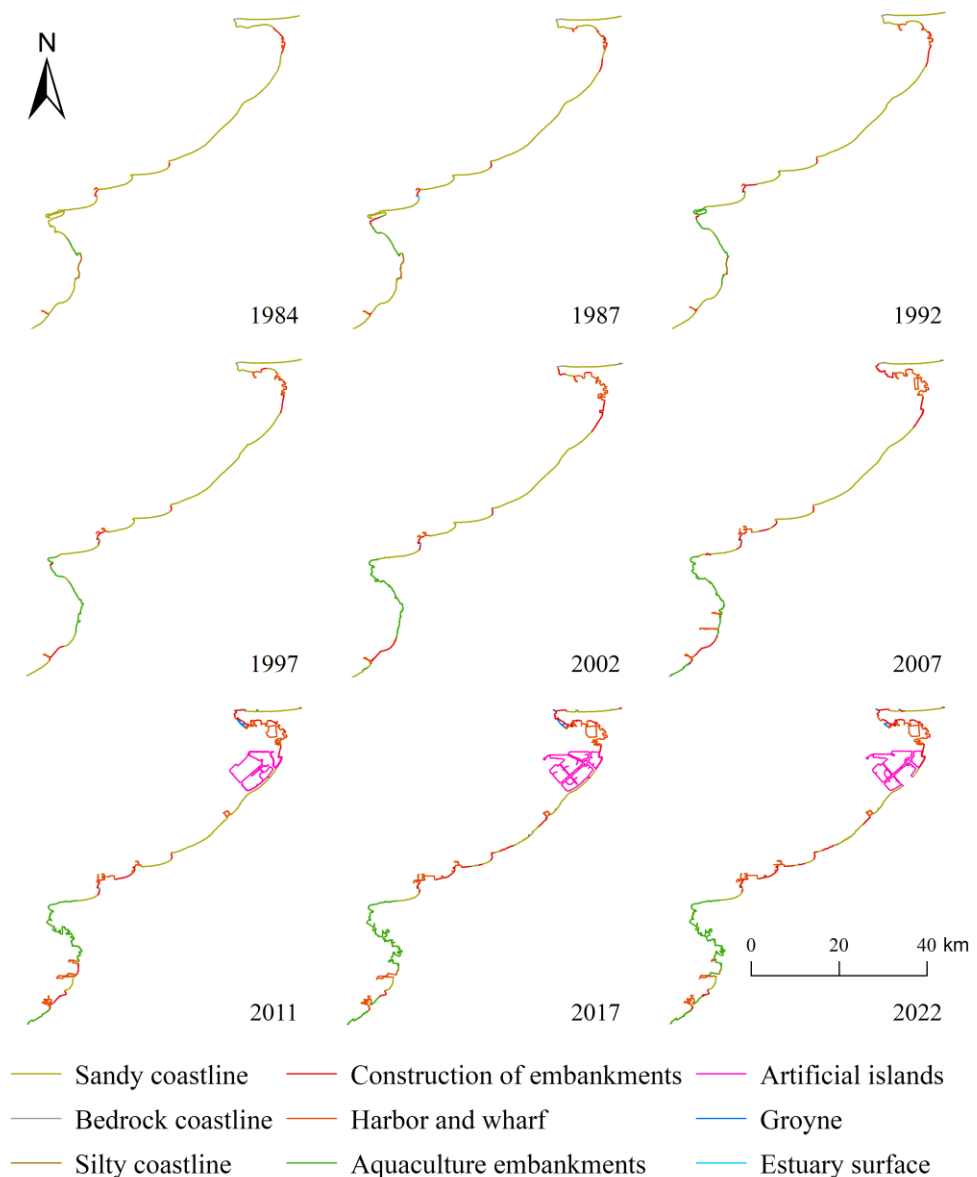


**Figure 4.** The spatiotemporal changes in the nine shoreline types between 1984 and 2022.

The presence of artificial coastal structures such as harbors, wharfs, and the construction of embankments, aquaculture embankments, and artificial islands have increased over the last 40 years.

An important growth has been seen in the last decade with the construction of the artificial island of Longkou, which began in 2011. The length of the new harbor and wharf increased from 12.22 km in 1984 to 98.45 km in 2022, an increase of 705.37%. The overall length of the outer edge of the Longkou Artificial Island increased from 86.18 km in 2011 to 106.08 km in 2017. In 2022, when the area was still under construction, the length of the artificial structures was reduced to 88.61 km due to reclamation activities.

The construction of embankments, mostly in Longkou Bay, Sanshan Island, and Shihu Mouth, have also increased by 444.44%, with the length increasing from 9.09 km in 1984 to 49.51 km in 2022.

The aquaculture areas, which are mainly located near Diaolongju, have led to an increase in the length of the embankments by 1015.63%, i.e., from 6.29 km in 1984 to 70.15 km in 2022. The construction of artificial groynes near residential areas from Longkou City to Sanshan Island became more frequent after 2007, and their development increased

from a total length of 1.11 km in 2007 to 12.22 km in 2017, with a reduction to 6.8 km in 2022. Finally, the coastline of estuaries has remained fairly constant and has changed significantly less compared to the other coastal types.

The overall distribution of the nine coastline types has changed considerably between 1984 and 2022 and the ICTD trend has increased (Figure 5). In the period 1984–1997, the proportion of sandy coasts, which almost always represents natural beaches, exceeded 50%, and human activities were relatively limited, resulting in a lower ICTD level. Over time, human activities increased, leading to a strong diversification of coastline types, with the proportions of various coastline types becoming more balanced and resulting in a gradual increase in ICTD.

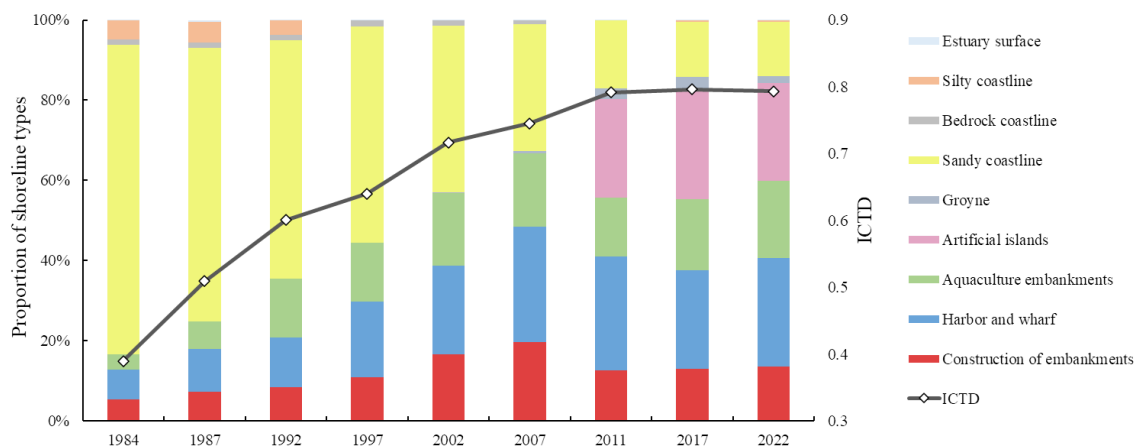


**Figure 5.** Evolution of the percentages of the nine coastlines types from 1984 to 2022 and its relationship with the ICTD.

### 3.3. Analysis of Coastline Change Rate

Looking at each of the nine intervals and for each of the nine coastline types, the LCI shows considerable variability between 1984 and 2022 (Table 2). The lowest change in coastlines relates to the period 1987–1992 with a LCI value of  $-0.31\%$ , while the highest value is between 2007 and 2011, resulting in a LCI value of  $17.24\%$ . The LCI calculated for all shorelines and for the entire period 1982–2022 is  $3.11\%$ .

**Table 2.** Length change intensity of different types of coastlines from 1984 to 2022.

Time Period	LCI/%									
	All Shorelines	Aquaculture Embankments	Construction of Embankments	Harbor and Wharf	Estuary Surface	Sandy Coastline	Silty Coastline	Bedrock Coastline	Groyne	Artificial Islands
1984–1987	0.45	27.68	11.36	16.34	120.29	-3.48	3.40	-1.02		
1987–1992	-0.31	22.32	2.71	2.97	-17.27	-2.87	-5.86	0.33		
1992–1997	0.25	0.46	6.49	10.33	-4.48	-1.64	-20.00	3.50		
1997–2002	1.66	6.45	12.96	5.56	28.10	-3.25		-2.81		
2002–2007	2.71	3.23	6.90	9.42	-5.89	-2.83		-0.92	58.68	
2007–2011	17.24	8.3	1.95	16.96	41.33	-2.22		-25.00	183.76	
2011–2017	1.78	5.77	2.38	-0.70	-9.37	-1.80			5.36	3.85
2017–2022	-1.21	0.44	-0.22	0.53	-12.28	-1.47	-0.03		-8.86	-3.29
1984–2022	3.11	26.73	11.70	18.56	-1.65	-1.63	-2.17			

The LCI for the coastal type with aquaculture embankments is  $26.73\%$  for the entire period 1984–2022. The highest value of  $27.68\%$  and the lowest of  $0.46\%$  relate to the periods 1984–1987 and 1992–1997, respectively. The LCI calculated between 1984 and 2022 for the coastal type with harbors and wharfs is  $18.56\%$ . The highest value of  $16.96\%$  refers to the period 2007–2011 and the lowest of  $0.53\%$  to the period 2017–2022. The coastal type protected by the construction of embankments has an LCI of  $11.70\%$  for 1984–2022. The highest LCI is for the period 1997–2002 with a value of  $12.96\%$  and the lowest for 2017–2022

with a value of  $-0.22\%$ . The LCI for the coastal type with artificial islands is  $3.85\%$  for the period 2011–2017 and  $-3.29\%$  for the subsequent period 2017–2022.

From 1984 to 2022, the LCI for sandy coastlines was consistently negative, with the greatest change occurring from 1984 to 1987 at  $-3.48\%$ , and the smallest change from 2017 to 2022 at  $-1.47\%$ . For silty coastline and bedrock coastline, the LCI was calculated only on the basis of the duration of their existence. The proportion of estuaries and groynes is relatively small, and their extent is correspondingly small.

Since the proportion of sandy coasts in the natural coastlines exceeds  $90\%$  each time, the accumulation and erosion processes on sandy shorelines were analyzed using EPR and LRR as key indicators of these processes to understand the development of sandy coasts.

By setting baselines and transects using DSAS, with a transect interval of  $100\text{ m}$ , the EPRs of sandy beaches were calculated in each of the nine periods (Figure 6). Positive and negative EPR values indicate that the sandy shoreline experienced accretion and erosion, respectively, while zero values indicate that no changes have taken place. The average EPR value at the intersection of all profile lines was calculated to reflect the overall change rate of the sandy shoreline during the specified period. The same method was used to calculate the LRR of sandy beaches overall from 1984 to 2022 (Figure 7).

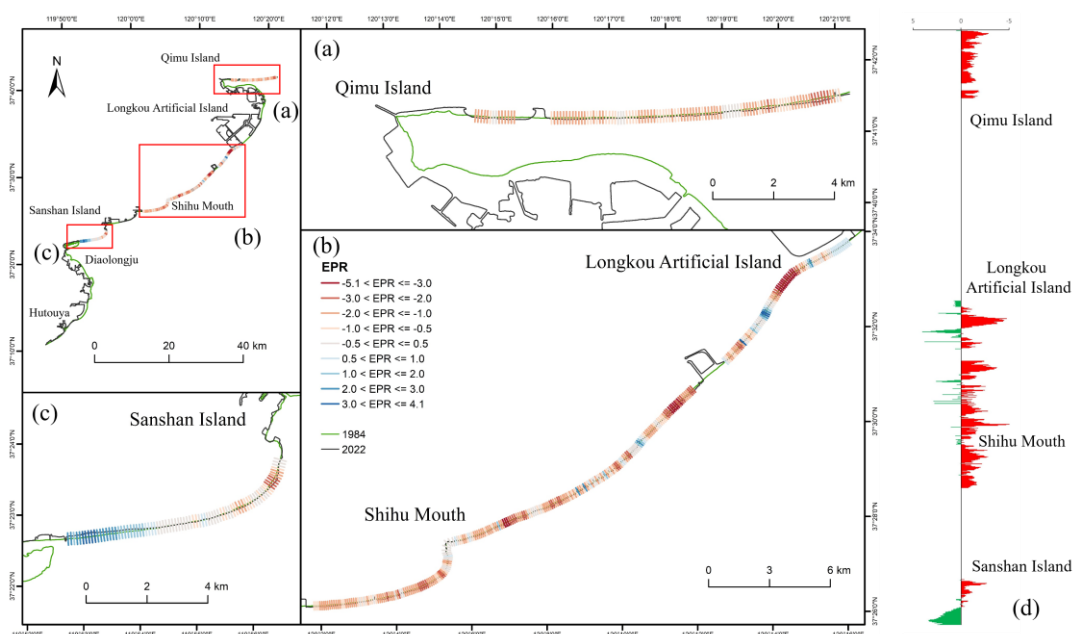


**Figure 6.** The EPR of the sandy shoreline from 1984 to 2022 in the (a) northern, (b) central, (c) southern of the survey area, and (d) rate of change ( $\text{m}\cdot\text{a}^{-1}$ ).

The results indicate that  $79.54\%$  of the sandy shoreline segments were affected by erosion between 1984–2022, while only  $20.08\%$  experienced accretion (Table 3) and  $0.38\%$  of them showed no significant change. The average erosion rate is  $-1.34\text{ m}\cdot\text{a}^{-1}$ , while the average accretion rate is  $1.20\text{ m}\cdot\text{a}^{-1}$ . The most severe period of erosion took place between 1997 and 2002, when  $79.88\%$  of the sandy coastline segments were affected. In the last decade, the construction of groynes has effectively mitigated erosion along the sandy shoreline, resulting in a transition from strong erosion to accretion in the surrounding sandy shoreline segments. Between 2017 and 2022, the percentage of accretion segments in the sandy shoreline reached  $74\%$ , which was significantly higher than that in other time periods (Table 3).

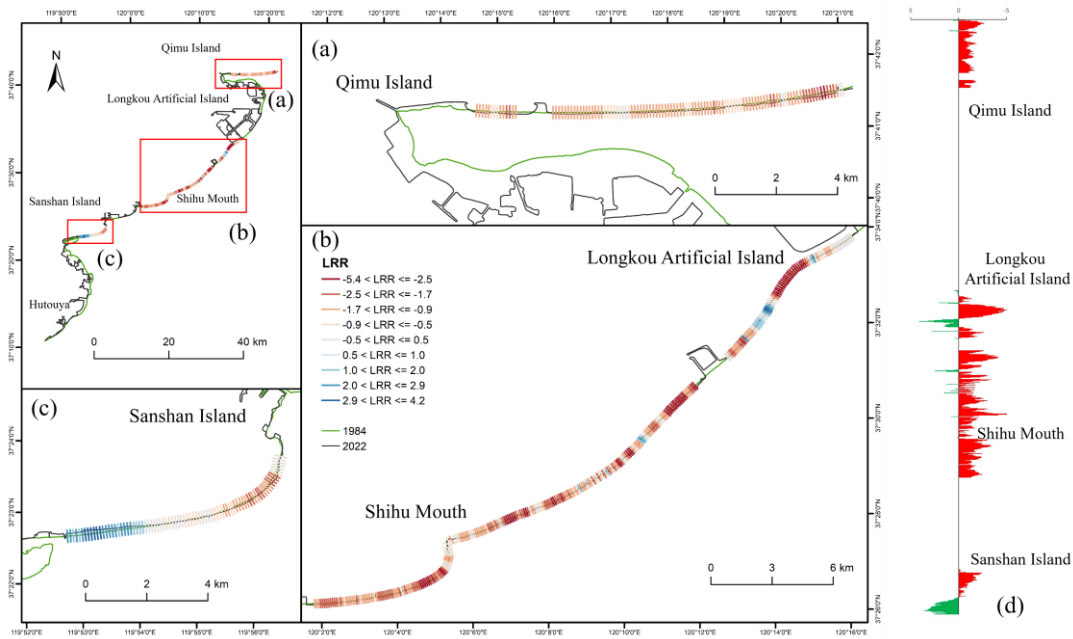


**Figure 7.** The LRR of the sandy shoreline from 1984 to 2022 in the (a) northern, (b) central, (c) southern of the survey area, and (d) rate of change ( $\text{m}\cdot\text{a}^{-1}$ ).

**Table 3.** EPR and LRR of the sandy shoreline from 1984 to 2022.

Time Period	Number of Profiles	Sedimentation Rate/ $(\text{m}\cdot\text{a}^{-1})$					Erosion Rate/ $(\text{m}\cdot\text{a}^{-1})$				Unchanged Proportion %	
		Maximum	Average	Median	Standard Deviation	Proportion %	Minimum Value	Average	Median	Standard Deviation		
1984–1987	933	27.22	8.11	7.35	5.26	71.28	−21.46	−6.94	−6.05	4.83	28.72	0.00
1987–1992	893	21.69	6.13	4.30	5.07	39.87	−18.81	−5.09	−4.43	3.66	59.80	0.33
1992–1997	820	36.39	5.00	3.67	5.00	57.07	−14.03	−3.21	−2.49	2.68	42.93	0.00
1997–2002	691	27.80	3.62	2.19	5.03	20.12	−26.63	−4.48	−3.88	3.21	79.88	0.00
EPR 2002–2007	634	8.61	2.11	1.69	1.66	36.75	−15.42	−3.39	−3.00	2.63	63.25	0.00
2007–2011	497	14.76	2.77	2.16	2.71	23.34	−29.25	−6.09	−4.77	5.28	76.66	0.00
2011–2017	476	25.85	3.71	2.43	4.12	25.84	−19.3	−4.94	−4.54	3.36	74.16	0.00
2017–2022	504	27.71	2.63	2.10	2.27	74.00	−6.02	−1.64	−1.25	1.45	25.60	0.40
LRR 1984–2022	513	4.05	1.20	0.71	1.05	20.08	−5.06	−1.34	−1.19	0.89	79.54	0.38
LRR 1984–2022	513	4.13	1.50	1.33	1.10	14.42	−5.34	−1.56	−1.4	1.00	85.58	0.00

The LRR results show that 85.58% of the sandy coastline segments experienced erosion between 1984 and 2022, while only 14.42% of the sandy coastline segments accreted. The average erosion rate is  $1.56 \text{ m}\cdot\text{a}^{-1}$ , while the average accretion rate is  $1.50 \text{ m}\cdot\text{a}^{-1}$ . Compared to the EPR, the LRR statistics show a higher percentage of sandy coastline segments experiencing erosion and a larger average erosion rate (Table 3).

### 3.4. Spatiotemporal Characteristics of the Fractal Dimension

The measure of the degree of geometric irregularity present in the coastline is assessed using fractal dimensions for the nine intervals. The highest fractal dimension is 1.0322 and refers to 2017, while the lowest is 1.0072 for 1992. The largest difference in coastline fractal dimensions is between 2011 and 2017, with a difference of 0.01. The smallest difference results pertain to the period of 1984–1987, with a difference of 0.0009. The linear regression between the length of the coastline and the fractal dimension (Figure 8) highlights a significant positive correlation with Pearson’s  $r$  value of 0.971.

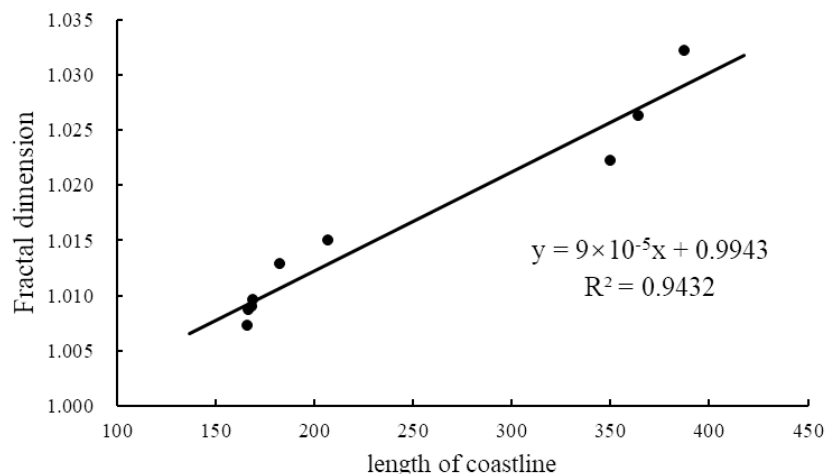


**Figure 8.** Analysis of the linear fit of shoreline length to fractal dimension.

Different types of coastlines have their own characteristics in terms of fractal dimensions. Rocky coastlines are the most irregular and have relatively high fractal dimensions. Artificial coastlines exhibit a regular pattern of bending over a large scale and straight lines over a small scale, with fractal dimensions lower than those of rocky coastlines. Sandy coastlines are generally formed by the accumulation of weathered small particles and exhibit slight curvatures but no prominent irregularities, resulting in the lowest fractal dimensions.

Since the study focuses mainly on sandy and artificial coasts, the variation in fractal dimensions reflects to some extent the changes in the length ratio of these two types of coastlines over time. Periods with significant changes in fractal dimensions correspond to periods of intense human activity that altered the natural morphology of the coastlines, resulting in new, more complex, and intricate coastlines. This lead to an increase or decrease in fractal dimensions, which is consistent with the mathematical definition of the fractal dimension.

### 3.5. Analysis of the Reasons for Coastline Changes

The 1984 and 2022 coastlines were compared, and the differences were interpreted and classified using remote sensing images (Figure 9). The results show that the eastern coastline of Laizhou Bay gained a land area of 12,025.42 hectares and experienced erosion of 261.21 hectares from 1984 to 2022. The anthropogenic factors that have contributed to the coastal changes between 1984 and 2022 include the construction of artificial islands, aquaculture facilities, ports, coastal sand mining, and other development projects. Natural factors include sea level changes and a decrease in sediment supply from rivers.

The coastlines of Longkou city, Sanshan Island, and the Diaolongju area have been significantly impacted by human activities. The construction of artificial islands, aquaculture embankments, and harbors have contributed most to the changes in the coastlines. From 1984 to 2022, these activities added 5802.73 hectares, 2846.27 hectares, and 1985.63 hectares, accounting for 47.04%, 23.07%, and 16.10% of the total changes, respectively. The increased construction land is mainly concentrated in Longkou City, with an additional area of 1351.20 hectares, accounting for 10.95% of the total changes. The newly added area of groynes is 49.67 hectares, accounting for 0.4% of the total area. The area from the Jie Reiver to Sanshan Island is mainly characterized by natural coastline. In this region, the coastline is experiencing natural erosion and deposition. From 1984 to 2022, the total area of erosion is 261.21 hectares, while the total area of deposition is 39.60 hectares, accounting for 2.12% and 0.32%, respectively (Table 4).

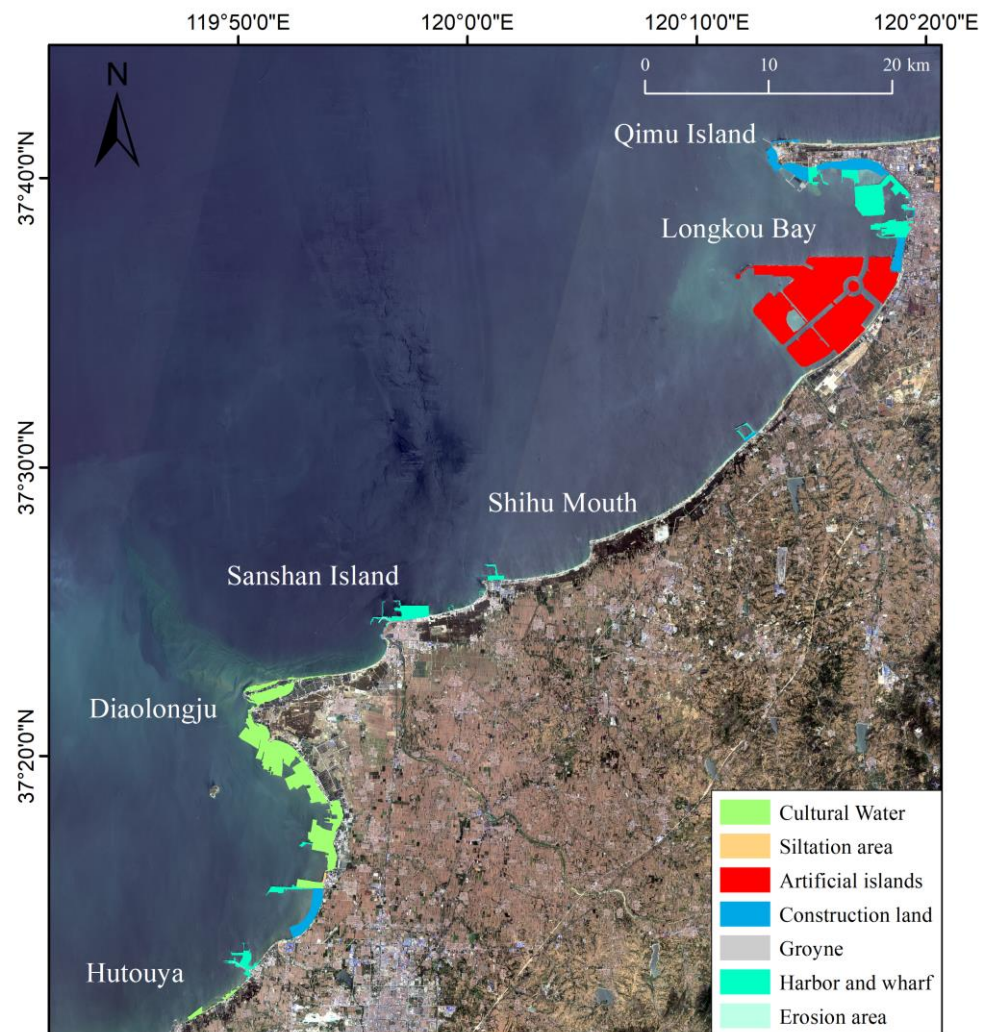


**Figure 9.** Coastal land–sea changes along the eastern coast of the Laizhou Bay from 1984 to 2022 (the background is a Sentinel-2 images from 2022).

**Table 4.** Coastal change types from 1984 to 2022.

Type	Human Activities				Natural Activities		
	Artificial Islands	Aquaculture Water Bodies	Harbor and Wharf	Construction Land	Groyne	Erosion	Accumulation
area/ha	5802.73	2846.27	1985.63	1351.20	49.67	261.21	39.60
percentage/%	47.04	23.07	16.10	10.95	0.40	2.12	0.32

The ICUD, which reflects the intensity of human activity development at different times (Figure 10), shows a consistent increase from 1984 to 2022, which was slow from 1984 to 2007 and fast between 2007 and 2011, while remaining relatively stable since 2011. Coastal aquaculture, port terminals, and other coastal activities have caused the coastline to expand unnaturally towards the sea. The speed and intensity of coastline changes are also much greater than natural shoreline development. Morphological changes in the coasts impacted by human activities have gone hand in hand with the socio-economic development of the surrounding cities.

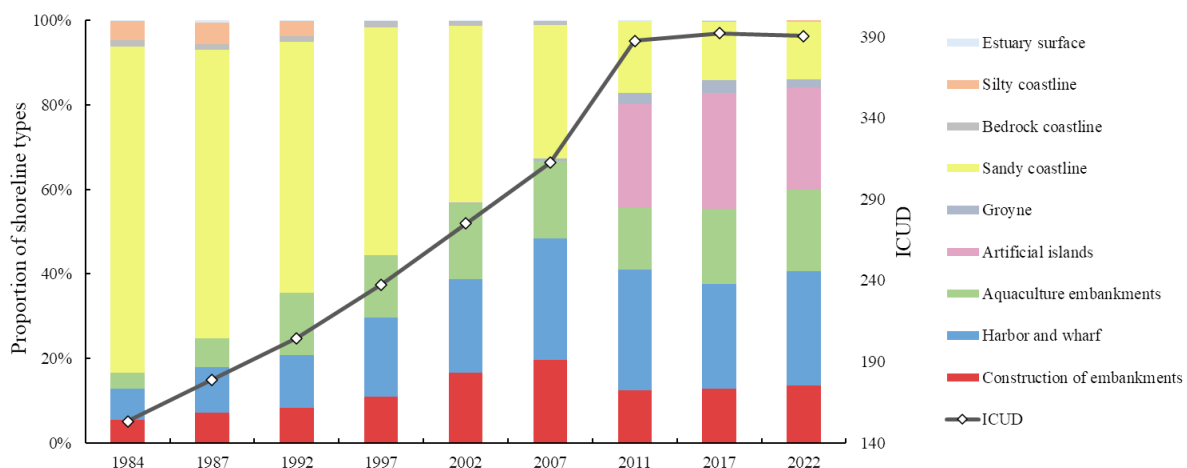


**Figure 10.** Evolution of the percentage of the nine coastline types from 1984 to 2022 and its relationship with ICUD by time from 1984 to 2022.

### 3.6. Prediction of Coastline Evolution

The data from the seven periods between 1984 and 2011 were imported into the Kalman filter and used to predict the variation in the sandy shore segment in the central sector of the study area in 2021. The predicted shoreline for 2021 was compared with the actual extracted shoreline for 2021 in the format given in Section 3.1 to validate the accuracy of the model's prediction. The results indicate that the percentage of shoreline predictions within a deviation range of less than 60 m from the actual measured shoreline is 94.31%. The percentage within 30 m is 59.72%, within 15 m is 28.93%, and within 10 m is 18.51%.

The 9-period coastline and its linear regression rate between 1984 and 2022 were used as the input data for initializing the Kalman filter. The predicted positions of the sandy coastline segments in 2023 are shown in Figure 11. Erosion and deposition between 2022 and 2032 were calculated for 1699 profiles positioned at 30 m intervals between the two coastlines. By 2032, 1437 profiles located in sandy coastline sections will be affected by erosion, which corresponds to 84.58% of the total number. The average erosion rate is  $-2.53 \text{ m}\cdot\text{a}^{-1}$ . Only 262 profile lines highlight sand sedimentation, accounting for 15.32% of the total. The average sedimentation rate is  $2.66 \text{ m}\cdot\text{a}^{-1}$ .

According to the prediction for 2032, the area from Longkou Artificial Island to Sanshan Island will be affected by significant erosion. This erosion is expected to be most severe on both sides of the Jie River, with an average coastline retreat of 90 m along the coastline. The southeastern section of Shihu Mouth will also be affected by significant erosion, and it is predicted that the coastline will retreat by 50 m between 2022 and 2032. The construction of the new harbor on Longkou Island, which changed the hydrodynamic conditions of the surrounding waters, will lead to significant erosion on the southwest side of the harbor. Relatively weak erosion is expected on the sandy shoreline on the right side of Qimu Island, as human activities in this area are relatively low and the coastline is less developed compared to other areas. From Diaolongju to Sanshan Island in the east, future changes to the coastline are expected to be relatively small. In particular, the sandy shoreline near Diaolongju will experience varying degrees of sedimentation in the next 10 years. This could be due to the presence of aquaculture ponds on the left side of this shoreline.

The erosion intensity of the shoreline increases towards Sanshan Island. The southern bank of the Wang River will experience the most severe erosion in the next 10 years. This can be attributed to the nearest coastal villages and towns, leading to frequent human activities. In addition, the construction of the Sanshan Island port has changed the direction of coastal currents and reduced the balance of sediment supply in the surrounding waters.

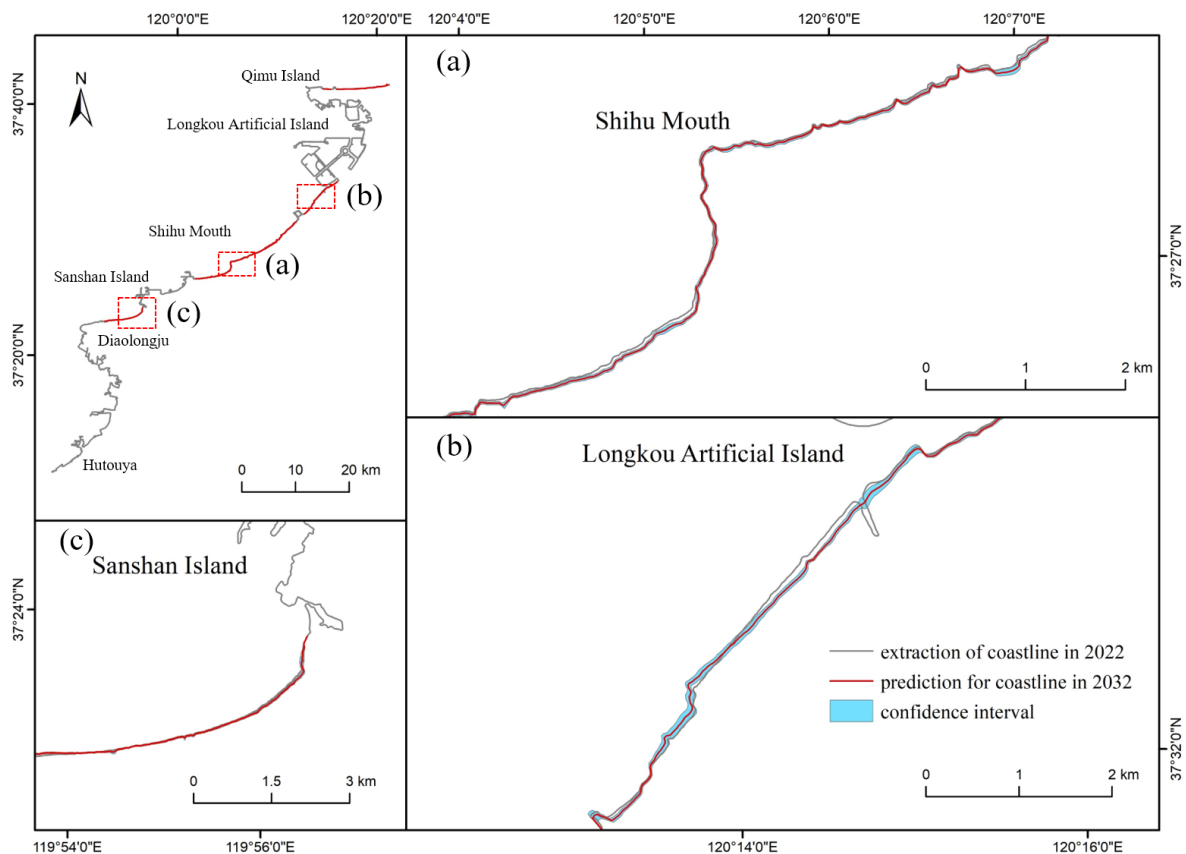


**Figure 11.** Prediction of the sandy coastline evolution in 2032 for (a) Shihu Mouth, (b) Longkou Artificial Island, (c) Sanshan Island.

#### 4. Discussion

In recent decades, many studies have addressed the environmental consequences of the rapid economic development of Laizhou Bay, most of them focusing on the problems of pollution and hydrogeological hazards [48–50]. The research on the changes in shoreline morphology lacks uniform standards for shoreline extraction, and the observation period is relatively short [27–29].

This study adopts a novel approach that captures shoreline changes at a regional scale and with high frequency during a long-term observation period. Impressive changes have been caused by the superimposition of anthropogenic activities and the resulting processes together with the effects of climate change. From 1984 to 2022, the coastal area of Laizhou Bay has expanded seaward by 12,025.42 hectares and eroded by 261.21 hectares (Table 4). These changes were accompanied by an increase of the shoreline length from 166.90 km to 364.20 km. All nine coastal types were affected, albeit to varying degrees, both in terms of percentage distribution and in the different time periods analyzed.

The expansion of coastal areas and the resulting increase in coastal length are the direct result of the ongoing anthropization of the Laizhou Bay, which includes the construction of new ports, wharf, piers, islands, embankments for coastal protection and aquaculture, and groynes in the Longkou Bay, Sanshan Island, Shihu Mouth, and Diaolongju areas. This statement is supported by the ICTD (Figure 5) and ICUD (Figure 10), which refer to the diversity of coast-line development patterns and the intensity of human activity development. Their quantification makes it clear that the changes on the Laizhou Bay coast have gone hand in hand with the socio-economic development of the surrounding cities. After a significant increase until 2011, coastal development remained almost stable until 2022. This status is also supported by the analysis of the rate of the change in the coastline

using the LCI and the analysis of the degree of geometric irregularity using the fractal dimension that show that both have the highest values between 2007 and 2011 (Table 2).

The new coastal structures altered the hydrodynamic environment of the former natural marine area, including tidal currents and waves, which disrupted the sediment balance and triggered erosion or deposition along the coast (Figure 9). The construction of the Longkou artificial island has resulted in an increase in the current velocity of the western coastal waters by 0.24–0.46 m/s [51]. A comparison of the coastal section west of the artificial island before and after construction shows that erosion was more severe than in previous cases.

The changes in the coastline are also due to the rapid development of coastal reclamation and aquaculture (Figure 9), the latter being driven by robust economic development and continued population growth [52]. According to the Yantai Statistical Yearbook for 2021, in the 37 years of China's opening-up from 1985 to 2021, the average growth rates of primary and secondary industries were 104.7% and 114.1%, respectively, the average growth rate of aquaculture production was 106.2%, and the average growth rate of port cargo throughput was 111.2%. Compared to other provinces, Shandong Province exhibits a higher intensity of coastal land reclamation, with beaches being converted into industrial and urban land on a large scale [53].

In addition to the causes described above, the changes in the shoreline can also be partly attributed to changes in sediment transport by the rivers, which are the main source of sand accumulation on the beaches along the east coast of Laizhou Bay. In the 1950s, the decline of forest cover on the Jiaozhou Peninsula to only 0.5% promoted the erosion of soil and topsoil in the upstream regions and the accumulation of sediments in the bay and on the beaches. The extensive construction of large-scale reservoirs from the 1950s to the 1960s caused a continuous decrease in sediment transport in the Jie River and has almost come to a complete standstill. This led to a shift in the balance of sediment supply along the coastline and triggered an erosion process [54]. The lack of sediment supply is consistent with the analysis of the coastline (Figure 4). In the period 1987–1992, the maximum retreat distance of the Jie River Estuary's shoreline reached an impressive 90.81 m and between 1992 and 1997, the coast reached the maximum retreat of an astounding 181.9 m.

Excessive sand mining on the beaches is another factor that caused the disruption of the balance of sediment along coastal area and contributes to shoreline erosion in the eastern coast of Laizhou Bay (Table 3). According to statistics, since 1982, 455 tons of sand have been mined annually on the Shandong Peninsula since 1982. In 1983, there were 67 large-scale sand mining sites along the coast, with a total sand mining volume of 695 tons per year. Although laws and regulations have been enacted in the region in recent years to strengthen ecological protection and promote sustainable economic development in relation to the extraction of sand and gravel resources, illegal sand mining activities persist. According to statistics, as of October 2023, there have been 13 cases of illegal sand mining in Zhaoyuan City (in the central area of the study area), ranking first in Shandong Province. Beach sand mining not only alters the shape of the beaches, but also increases the depth of the water in the nearshore, resulting in greater wave energy and increasing erosion.

Sea level rise and land subsidence are both processes that lead to the elevation loss of the coastal area with respect to the mean sea level. These processes caused an upward migration of nearshore underwater slopes and increased wave energy and the amount of sand transported from the beaches into the sea, leading to coastal erosion. The effects of sea level rise often unfold slowly and persist over a long period of time in the Laizhou Bay [55]. According to the "2022 China sea level bulletin", the sea level on the Chinese coasts rose at a rate of  $3.5 \text{ mm} \cdot \text{a}^{-1}$  from 1980 to 2021. In 2022, the sea level was 94 mm higher than the average year and the Laizhou Bay experienced the highest sea level rise since 1980, with a deviation of 108 mm from the average. Based on an analysis of the actual morphology of the beaches on the eastern coast of Laizhou Bay, the estimated shoreline retreat sea level rise is  $45 \text{ mm} \cdot \text{a}^{-1}$ . Leatherman et al., and a sea level rise of 108 mm would result in an average shoreline erosion of approximately 16.2 m [56]. Although these data suggest that

sea level rise does indeed affect the morphology of the eastern coast of Laizhou Bay, leading to gradual shoreline erosion, it is not the primary driver driving of the shoreline erosion in this area.

The Kalman filter has shown good applicability in predicting regional coastline changes by 2032. However, the model did not account for the effects of the expected relative sea level rise and therefore underestimated erosion. For example, coastal mineral extraction, aquaculture, and reclamation cause varying degrees of land subsidence, which can be up to  $1\text{--}3\text{ cm}\cdot\text{a}^{-1}$  [57,58]. Liu et al. [59] calculated a sea level rise trend of about  $5\text{ mm}\cdot\text{a}^{-1}$  (for the period 1980–2015) in Bohai Bay due to global climate change. Therefore, the erosion of  $2.53\text{ m}\cdot\text{a}^{-1}$  predicted by 2032, which will affect 84.58% of today's sandy coast, will be greater. Note also that sea level rise simultaneously undermines the effectiveness of seawalls and alters sediment transport along the coasts [59,60]. Appropriate planning measures will be crucial to mitigate the future erosion of the Laizhou Bay coastline [61,62].

## 5. Conclusions

This study proposes an innovative approach to studying coastline changes by quantifying a set of morphological indicators at a regional scale and with high temporal frequency over a long observation period. GEE has been used to extract coastline positions every 5 years from 1984 to 2022 in the eastern coast of Laizhou Bay (China). Impressive changes have been observed on the coasts, the causes of which are attributed to the overlap of anthropogenic activities and the induced associated processes with the effects of climate change. The main conclusions are as follows:

- The coastal area expanded seaward by 12,025.42 hectares and eroded by 261.21 hectares, resulting in an increase in coastal length from 166.90 km to 364.20 km. All types of coasts were affected, although to varying degrees, both in terms of percentage distribution and over the different time periods analyzed.
- The proportion of the natural coast continuously decreased leading to an increasing diversity of coastline types over the whole observation period.
- Coastline diversity and the intensity of the development of human activity show a consistent increase from 1984 to 2022, which was slow from 1984 to 2007 and fast between 2007 and 2011, while remaining relatively stable since 2011.
- The change in the intensity of the coastline between 1984 and 2022 is 3.11%. The highest value is 17.24% and relates to the period 2007–2011.
- The fractal dimension of the coastline showed an upward trend between 1984 and 2022. A positive correlation with the length of the coastline indicates the influence of human activities on the changes in the coastline.
- In the coastal erosion recorded in 2022, the proportion of sandy coastline erosion calculated by EPR is 79.54%, while the proportion calculated by LRR is 85.59%, which indicates a severe extent, especially in the central part, where natural factors and human intervention interact.
- The prediction of coastline evolution by 2023 shows that 84.58% of the sandy coastal sections will be affected by varying degrees of erosion, with the most severe condition being reached at a retreat rate of  $-2.53\text{ m}\cdot\text{a}^{-1}$ . Conversely, only 15.32% of sandy beaches will increase due to sedimentation, with the progradation rate reaching  $2.66\text{ m}\cdot\text{a}^{-1}$ .

**Author Contributions:** Conceptualization, K.M. and C.T.; methodology, K.M.; software, K.M., C.T. and X.Z.; validation, Y.L., J.S. and J.L.; formal analysis, K.M.; investigation, J.S.; resources, X.G.; data curation, K.M.; writing—original draft preparation, K.M.; writing—review and editing, X.Z., L.T. and Y.L.; visualization, S.D.; supervision, X.G.; project administration, Y.L.; funding acquisition, C.T. All authors have read and agreed to the published version of the manuscript.

**Funding:** This work was supported by the National Natural Science Foundation of China (U2106211), the Key Program of National Science Foundation (No. 41530966) and the seed project of Yantai Institute of Coastal Zone Research, Chinese Academy of Sciences (Grant No. YIC E351030601).

**Data Availability Statement:** Data associated with this research are available and can be obtained by contacting the corresponding author.

**Acknowledgments:** This study was carried out with the support of the 2020–2022 Scientific Cooperation Program between the National Research Council of Italy and the Chinese Academy of Sciences, Project “Coastal system changes over the Anthropocene: Natural vs Induced drivers”. The authors thank the editors and reviewers for their helpful comments and valuable suggestions that greatly improved the paper.

**Conflicts of Interest:** The authors declare no conflict of interest.

## References

1. Boak, E.H.; Turner, I.L. Shoreline Definition and Detection: A Review. *J. Coast. Res.* **2005**, *21*, 688–703. [[CrossRef](#)]
2. Adu, K.; Emmanuel, M.A.; Kwaku, K.-K.; Osman, A. Socio—Economic Impact of Lake Bosomtwe Shoreline Changes on Catchment Residents in Ghana. *Int. J. Sci. Res. Publ.* **2014**, *4*, 1–7.
3. Paterson, S.K.; O’Donnell, A.; Loomis, D.K.; Hom, P. *The Social and Economic Effects of Shoreline Change: North Atlantic, South Atlantic, Gulf of Mexico, and Great Lakes Regional Overview*; Eastern Research Group Inc: Lexington, MA, USA, 2010.
4. Guimaraes, M.; Zúñiga-Ríos, A.; Cruz-Ramírez, C.J.; Chávez, V.; Odériz, I.; Van Tussenbroek, B.I.; Silva, R. The Conservational State of Coastal Ecosystems on the Mexican Caribbean Coast: Environmental Guidelines for Their Management. *Sustainability* **2021**, *13*, 2738. [[CrossRef](#)]
5. Moussa, M.; Baccar, L.; Ben Khemis, R. La lagune de Ghar El Melh: Diagnostic écologique et perspectives d’aménagement hydraulique. *Rev. Sci. L’eau* **2005**, *18*, 13–26. [[CrossRef](#)]
6. Nichols, C.R.; Zinnert, J.; Young, D.R. Degradation of Coastal Ecosystems: Causes, Impacts and Mitigation Efforts. In *Tomorrow’s Coasts Complex Impermanent*; Springer: Cham, Switzerland, 2019; pp. 119–136.
7. Lewin, W.-C.; Mehner, T.; Ritterbusch, D.; Brämick, U. The Influence of Anthropogenic Shoreline Changes on the Littoral Abundance of Fish Species in German Lowland Lakes Varying in Depth as Determined by Boosted Regression Trees. *Hydrobiologia* **2014**, *724*, 293–306. [[CrossRef](#)]
8. Anderson, A.; Ratas, U.; Ravis, R.; Palginõmm, V. Relationship between Coastline Changes and Dynamics of Coastal Ecosystems of Tahkuna Peninsula, Estonia. In Proceedings of the 2012 IEEE/OES Baltic International Symposium (BALTIC), Klaipeda, Lithuania, 8–10 May 2012; pp. 1–6.
9. Manyama, M.T.; Hepelwa, A.S.; Nahonyo, C.L. Analysis of Socio-Ecological Impacts of Built Environment at Dar Es Salaam Metropolitan Coastline, Tanzania. *Open J. Soc. Sci.* **2019**, *07*, 161–182. [[CrossRef](#)]
10. Li, J.; Liu, Y.; Pu, R.; Yuan, Q.; Shi, X.; Guo, Q.; Song, X. Coastline and Landscape Changes in Bay Areas Caused by Human Activities: A Comparative Analysis of Xiangshan Bay, China and Tampa Bay, USA. *J. Geogr. Sci.* **2018**, *28*, 1127–1151. [[CrossRef](#)]
11. Bailey, G.N.; King, G.C. Dynamic Landscapes and Human Dispersal Patterns: Tectonics, Coastlines, and the Reconstruction of Human Habitats. *Quat. Sci. Rev.* **2011**, *30*, 1533–1553. [[CrossRef](#)]
12. Petrișor, A.-I.; Hamma, W.; Nguyen, H.D.; Randazzo, G.; Muzirafuti, A.; Stan, M.-I.; Tran, V.T.; Aștefănoaiei, R.; Bui, Q.-T.; Vintilă, D.-F. Degradation of Coastlines under the Pressure of Urbanization and Tourism: Evidence on the Change of Land Systems from Europe, Asia and Africa. *Land* **2020**, *9*, 275. [[CrossRef](#)]
13. Appeaning Addo, K.; Jayson-Quashigah, P.N.; Kufogbe, K.S. Quantitative Analysis of Shoreline Change Using Medium Resolution Satellite Imagery in Keta, Ghana. *Mar. Sci.* **2012**, *1*, 1–9. [[CrossRef](#)]
14. Cazenave, A.; Cozannet, G.L. Sea Level Rise and Its Coastal Impacts. *Earth’s Future* **2014**, *2*, 15–34. [[CrossRef](#)]
15. Shalaby, A.; Tateishi, R. Remote Sensing and GIS for Mapping and Monitoring Land Cover and Land-Use Changes in the Northwestern Coastal Zone of Egypt. *Appl. Geogr.* **2007**, *27*, 28–41. [[CrossRef](#)]
16. Muttitanon, W.; Tripathi, N.K. Land Use/Land Cover Changes in the Coastal Zone of Ban Don Bay, Thailand Using Landsat 5 TM Data. *Int. J. Remote Sens.* **2005**, *26*, 2311–2323. [[CrossRef](#)]
17. Esteves, L.; Williams, J.; Nock, A.; Lymbery, G. Quantifying Shoreline Changes along the Sefton Coast (UK) and the Implications for Research-Informed Coastal Management. *J. Coast. Res.* **2009**, 602–606.
18. Cenci, L.; Disperati, L.; Persichillo, M.G.; Oliveira, E.R.; Alves, F.L.; Phillips, M. Integrating Remote Sensing and GIS Techniques for Monitoring and Modeling Shoreline Evolution to Support Coastal Risk Management. *GISci. Remote Sens.* **2018**, *55*, 355–375. [[CrossRef](#)]
19. Mahrad, B.E.; Newton, A.; Icely, J.D.; Kacimi, I.; Abalansa, S.; Snoussi, M. Contribution of Remote Sensing Technologies to a Holistic Coastal and Marine Environmental Management Framework: A Review. *Remote Sens.* **2020**, *12*, 2313. [[CrossRef](#)]
20. Lodato, F.; Colonna, N.; Pennazza, G.; Praticò, S.; Santonico, M.; Vollero, L.; Pollino, M. Analysis of the Spatiotemporal Urban Expansion of the Rome Coastline through GEE and RF Algorithm, Using Landsat Imagery. *ISPRS Int. J. Geo-Inf.* **2023**, *12*, 141. [[CrossRef](#)]
21. Arjasakusuma, S.; Kusuma, S.S.; Saringatin, S.; Wicaksono, P.; Mutaqin, B.W.; Rafif, R. Shoreline Dynamics in East Java Province, Indonesia, from 2000 to 2019 Using Multi-Sensor Remote Sensing Data. *Land* **2021**, *10*, 100. [[CrossRef](#)]

22. Ding, Y.; Yang, X.; Jin, H.; Wang, Z.; Liu, Y.; Liu, B.; Zhang, J.; Liu, X.; Gao, K.; Meng, D. Monitoring Coastline Changes of the Malay Islands Based on Google Earth Engine and Dense Time-Series Remote Sensing Images. *Remote Sens.* **2021**, *13*, 3842. [[CrossRef](#)]
23. Maiti, S.; Bhattacharya, A.K. Shoreline Change Analysis and Its Application to Prediction: A Remote Sensing and Statistics Based Approach. *Mar. Geol.* **2009**, *257*, 11–23. [[CrossRef](#)]
24. Hamzaoglu, C.; Dihkan, M. Automatic Extraction of Highly Risky Coastal Retreat Zones Using Google Earth Engine (GEE). *Int. J. Environ. Sci. Technol.* **2023**, *20*, 353–368. [[CrossRef](#)]
25. Wang, X.; Xiao, X.; Zou, Z.; Chen, B.; Ma, J.; Dong, J.; Doughty, R.B.; Zhong, Q.; Qin, Y.; Dai, S. Tracking Annual Changes of Coastal Tidal Flats in China during 1986–2016 through Analyses of Landsat Images with Google Earth Engine. *Remote Sens. Environ.* **2020**, *238*, 110987. [[CrossRef](#)] [[PubMed](#)]
26. Bishop-Taylor, R.; Nanson, R.; Sagar, S.; Lymburner, L. Mapping Australia’s Dynamic Coastline at Mean Sea Level Using Three Decades of Landsat Imagery. *Remote Sens. Environ.* **2021**, *267*, 112734. [[CrossRef](#)]
27. Xu, Y.; Gao, H.; Wei, X.; Zhu, J. The Effects of Reclamation Activity and Yellow River Runoff on Coastline and Area of the Laizhou Bay, China. *J. Ocean Univ. China* **2021**, *20*, 729–739. [[CrossRef](#)]
28. Liu, C.; Chang, J.; Chen, M.; Zhang, T. Dynamic Monitoring and Its Influencing Factors Analysis of Coastline in the Laizhou Bay since 1985. *J. Coast. Res.* **2020**, *105*, 18–22. [[CrossRef](#)]
29. Jian, W.; Junqiang, Z.; Zhiqian, G.; Yameng, L.; Ying, G. Coastal Evolution of Southern Coast of Laizhou Bay during 1973–2016 and Maintenance Countermeasures. *Mar. Geol. Front.* **2019**, *35*, 27–36.
30. Weifu, S.; Jie, Z.; Guangbo, R.; Yi, M.; Shaoqi, N. *Coastline Remote Sensing Monitoring and Change Analysis of Laizhou Bay from 1978 to 2009*; Atlantis Press: Amsterdam, The Netherlands, 2013; pp. 38–41.
31. Kalman, R.E. A New Approach to Linear Filtering and Prediction Problems. *J. Basic Eng.* **1960**, *82*, 35–45. [[CrossRef](#)]
32. Long, J.W.; Plant, N.G. Extended Kalman Filter Framework for Forecasting Shoreline Evolution. *Geophys. Res. Lett.* **2012**, *39*, L13603–L13608. [[CrossRef](#)]
33. Vos, K.; Splinter, K.D.; Harley, M.D.; Simmons, J.A.; Turner, I.L. CoastSat: A Google Earth Engine-Enabled Python Toolkit to Extract Shorelines from Publicly Available Satellite Imagery. *Environ. Model. Softw.* **2019**, *122*, 104528. [[CrossRef](#)]
34. Tu, T.-M.; Su, S.-C.; Shyu, H.-C.; Huang, P.S. A New Look at IHS-like Image Fusion Methods. *Inf. Fusion* **2001**, *2*, 177–186. [[CrossRef](#)]
35. Xu, H. Modification of Normalised Difference Water Index (NDWI) to Enhance Open Water Features in Remotely Sensed Imagery. *Int. J. Remote Sens.* **2006**, *27*, 3025–3033. [[CrossRef](#)]
36. Otsu, N. A Threshold Selection Method from Gray-Level Histograms. *IEEE Trans. Syst. Man Cybern.* **1979**, *9*, 62–66. [[CrossRef](#)]
37. Cipolletti, M.P.; Delrieux, C.A.; Perillo, G.M.E.; Cintia Piccolo, M. Superresolution Border Segmentation and Measurement in Remote Sensing Images. *Comput. Geosci.* **2012**, *40*, 87–96. [[CrossRef](#)]
38. Carrere, L.; Lyard, F.; Cancet, M.; Guillot, A. FES 2014, a New Tidal Model on the Global Ocean with Enhanced Accuracy in Shallow Seas and in the Arctic Region. In Proceedings of the EGU General Assembly Conference Abstracts, Vienna, Austria, 12–17 April 2015; p. 5481.
39. Wu, T. Analysis of Spatio-Temporal Characteristics of Mainland Coastline Changes in China in Nearly 70 Years. Ph.D. Thesis, Yantai Institute of Coastal Zone Research, Chinese Academy of Sciences, Beijing, China, 2016. (In Chinese)
40. Xu, J.; Zhang, Z.; Zhao, X.; Wen, Q.; Zuo, L.; Wang, X.; Yi, L. Spatial-temporal analysis of coastline changes in northern China from 2000 to 2012. *Acta Geogr. Sin.* **2013**, *68*, 651–660. (In Chinese)
41. Dolan, R.; Fenster, M.S. Temporal Analysis of Shoreline Recession and Accretion. *J. Coast. Res.* **1991**, *7*, 723–744.
42. Zeinali, S.; Talebbeydokhti, N.; Dehghani, M. Spatiotemporal Shoreline Change in Boushehr Province Coasts, Iran. *J. Ocean Limnol.* **2020**, *38*, 707–721. [[CrossRef](#)]
43. Himmelstoss, E.A.; Henderson, R.E.; Kratzmann, M.G.; Farris, A.S. *Digital Shoreline Analysis System (DSAS) Version 5.0 User Guide*; US Geological Survey: Reston, VA, USA, 2018. [[CrossRef](#)]
44. Wu, T.; Hou, X.; Xu, X. Spatio-Temporal Characteristics of the Mainland Coastline Utilization Degree over the Last 70 Years in China. *Ocean Coast. Manag.* **2014**, *98*, 150–157. [[CrossRef](#)]
45. Mandelbrot, B. How Long Is the Coast of Britain? Statistical Self-Similarity and Fractional Dimension. *Science* **1967**, *156*, 636–638. [[CrossRef](#)] [[PubMed](#)]
46. Ludeman, L.C. *Random Processes: Filtering, Estimation, and Detection*; John Wiley & Sons, Inc.: Hoboken, NJ, USA, 2003; ISBN 0-471-25975-6.
47. Liu, C.; Shi, R.X.; Zhang, Y.H.; Shen, Y.; Ma, J.H.; Wu, L.Z.; Doko, T.; Chen, L.J.; Lv, T.T.; Tao, Z.; et al. 2015: How Many Islands (Isles, Rocks), How Large Land Areas and How Long of Shorelines in the World?—Vector Data Based on Google Earth Images. *J. Glob. Change Data Discov.* **2019**, *3*, 124–148.
48. Sun, Y.; Xu, S.; Wang, Q.; Hu, S.; Qin, G.; Yu, H. Response of a Coastal Groundwater System to Natural and Anthropogenic Factors: Case Study on East Coast of Laizhou Bay, China. *Int. J. Environ. Res. Public Health.* **2020**, *17*, 5204. [[CrossRef](#)]
49. Gao, X.; Zhuang, W.; Chen, C.-T.A.; Zhang, Y. Sediment Quality of the SW Coastal Laizhou Bay, Bohai Sea, China: A Comprehensive Assessment Based on the Analysis of Heavy Metals. *PLoS ONE* **2015**, *10*, e0122190. [[CrossRef](#)] [[PubMed](#)]
50. Donnici, S.; Serandrei-Barbero, R.; Gao, X.; Tang, C.; Tosi, L. Utilizing Benthic Foraminifera to Explore the Environmental Condition of the Laizhou Bay (Bohai Sea, China). *Mar. Pollut. Bull.* **2021**, *167*, 112323. [[CrossRef](#)] [[PubMed](#)]

51. Yu, X.; Wang, Z.; Leng, X.; Liu, D.; Yang, X.; Zhang, Q.; Li, A. Effects of Mariculture on Hydrodynamic Conditions in Laizhou Bay. *Period. Ocean. Univ. China* **2022**, *52*, 132–139. (In Chinese) [[CrossRef](#)]
52. Tian, B.; Wu, W.; Yang, Z.; Zhou, Y. Drivers, Trends, and Potential Impacts of Long-Term Coastal Reclamation in China from 1985 to 2010. *Estuar. Coast. Shelf Sci.* **2016**, *170*, 83–90. [[CrossRef](#)]
53. Gong, M.; Wu, X.; Yu, L. Reclamation Dynamics Along the Mainland Coast of Shandong Province during 1974–2017. *J. Geo-Inf. Sci.* **2019**, *21*, 1911–1922. (In Chinese) [[CrossRef](#)]
54. Zhan, C.; Yu, J.; Wang, Q.; Su, Y.; Zhou, D. Spatial and Temporal Dynamics of Sandy Coastal Geomorphology in The East of Laizhou Bay Over Recent 60 Years. *Acta Oceanol. Sin.* **2017**, *39*, 90–100. (In Chinese) [[CrossRef](#)]
55. Zhuang, Z.; Lin, Z.; Liu, Z.; Deng, X. Sea Level Changes and Coastal Responses. *Mar. Geol. Lett.* **2003**, *19*, 1–12. (In Chinese) [[CrossRef](#)]
56. Leatherman, S.P.; Zhang, K.; Douglas, B.C. Sea Level Rise Shown to Drive Coastal Erosion. *Eos Trans. Am. Geophys. Union* **2000**, *81*, 55–57. [[CrossRef](#)]
57. Peng, M.; Zhao, C.; Zhang, Q.; Lu, Z.; Bai, L.; Bai, W. Multi-Scale and Multi-Dimensional Time Series InSAR Characterizing of Surface Deformation over Shandong Peninsula, China. *Appl. Sci.* **2020**, *10*, 2294. [[CrossRef](#)]
58. Quanyuan, W.; Jiewu, P.; Shanzhong, Q.; Yiping, L.; Congcong, H.; Tingxiang, L.; Limei, H. Impacts of Coal Mining Subsidence on the Surface Landscape in Longkou City, Shandong Province of China. *Environ. Earth Sci.* **2009**, *59*, 783–791. [[CrossRef](#)]
59. Liu, K.-X.; Wang, H.; Fu, S.-J.; Gao, Z.-G.; Dong, J.-X.; Feng, J.-L.; Gao, T. Evaluation of Sea Level Rise in Bohai Bay and Associated Responses. *Adv. Clim. Change Res.* **2017**, *8*, 48–56. [[CrossRef](#)]
60. Li, Y.; Zhang, H.; Tang, C.; Zou, T.; Jiang, D. Influence of Rising Sea Level on Tidal Dynamics in the Bohai Sea. *J. Coast. Res.* **2016**, *74*, 22–31. [[CrossRef](#)]
61. Harris, L.R.; Bessinger, M.; Dayaram, A.; Holness, S.; Kirkman, S.; Livingstone, T.-C.; Lombard, A.T.; Lück-Vogel, M.; Pfaff, M.; Sink, K.J.; et al. Advancing Land-Sea Integration for Ecologically Meaningful Coastal Conservation and Management. *Biol. Conserv.* **2019**, *237*, 81–89. [[CrossRef](#)]
62. Annis, G.M.; Pearsall, D.R.; Kahl, K.J.; Washburn, E.L.; May, C.A.; Franks Taylor, R.; Cole, J.B.; Ewert, D.N.; Game, E.T.; Doran, P.J. Designing Coastal Conservation to Deliver Ecosystem and Human Well-Being Benefits. *PLoS ONE* **2017**, *12*, e0172458. [[CrossRef](#)] [[PubMed](#)]

**Disclaimer/Publisher’s Note:** The statements, opinions and data contained in all publications are solely those of the individual author(s) and contributor(s) and not of MDPI and/or the editor(s). MDPI and/or the editor(s) disclaim responsibility for any injury to people or property resulting from any ideas, methods, instructions or products referred to in the content.